

# 3-Dimensional microstructural characterization of CdTe absorber layers from CdTe/CdS thin film solar cells

Guillaume Stechmann<sup>a,\*</sup>, Stefan Zaefferer<sup>a</sup>, Peter Konijnenberg<sup>a</sup>, Dierk Raabe<sup>a</sup>,  
Christina Gretener<sup>b</sup>, Lukas Kranz<sup>b</sup>, Julian Perrenoud<sup>b</sup>, Stephan Buecheler<sup>b</sup>,  
Ayodhya Nath Tiwari<sup>b</sup>

<sup>a</sup> Max-Planck-Institut Für Eisenforschung GmbH, Max-Planck-Straße 1, 40237 Düsseldorf, Germany

<sup>b</sup> Empa – Swiss Federal Laboratories for Materials Science and Technology, Überlandstrasse 129, 8600 Dübendorf, Switzerland

## ARTICLE INFO

### Article history:

Received 26 August 2015

Received in revised form

12 January 2016

Accepted 27 February 2016

Available online 22 March 2016

### Keywords:

CdTe

EBSD

Grain boundary

Microstructure

Thin film

Growth

## ABSTRACT

The present work reports on a study on the microstructure and its evolution during processing of CdTe absorber layers from CdTe/CdS thin film solar cells grown by low-temperature processes in substrate configuration. Investigations were performed at different stages of the cell manufacturing, from deposition to the final functional solar cell, with the aim to understand the microstructure formation of the photoactive layer. To this end 3-dimensional microstructure characterization was performed using focused ion beam/electron backscatter diffraction tomography ("3D-EBSD") together with conventional 2D-EBSD. The analyses revealed strong microstructural and textural changes developing across the thickness of the absorber material, between the back contact and the p–n junction interfaces. Based on the 3-dimensional reconstruction of the CdTe thin film, a coherent growth model was proposed, emphasizing the microstructural continuity before and after a typical CdCl<sub>2</sub>-annealing activation treatment. One of the principal results is that the absorber layer is created by two concomitant processes, deposition and recrystallization, which led to different textures and microstructures. Further changes are the result of subsequent annealing treatments, favoring twinning and promoting well-defined texture components. The results open the possibility for a grain boundary engineering approach applied to the design of such cells.

© 2016 Elsevier B.V. All rights reserved.

## 1. Introduction

Cadmium telluride (CdTe) layers are efficiently used for solar energy conversion in the form of thin film solar cells. Their particularly well-fitting optoelectronic properties (almost ideal bandgap, high absorption coefficient and high thermal stability [1,2]) are still driving the interests of both scientific communities and industrial companies in the highly competitive world of photovoltaic materials.

Recent developments of new thin-film deposition processes and a better understanding of the material's electronic properties enabled an important advance in the efficiency of such cells; increasing from 10% in 1972 [3] to 22.1% in 2016. Nevertheless, the low values of the achievable open circuit voltages (around 900 mV) remain problematic towards efficiency improvements. The dependency of this parameter on the dopant density and the minority carrier concentration emphasizes the crucial role of

crystallographic defects in CdTe-based cell efficiency [4,5]. Indeed, grain boundaries, as one of the most frequent and prominent defects in CdTe absorber layers, may act as diffusion pathways for dopants. At the same time, they affect the carriers lifetime in a way which remains, however, ambiguous [6–9]. A number of publications indicate that grain boundaries create deep energy levels in the band gap, leading to a local enhancement of detrimental Shockley–Read–Hall (i.e. trap-assisted) recombinations due to the presence of wrong or dangling bonds at these interfaces [10–11]. Furthermore, local disruptions of the long range order have also been proposed to result in a band bending confined to the grain boundaries. The exact resulting band structure is, nonetheless, still disputed. On the one hand, Woods et al. [8] proposed a double-barrier model with a minority carrier barrier in the surroundings of the boundary while the grain boundary core would repel majority carriers. On the other hand, Galloway et al. [12] and Durose et al. [13] proposed a single-barrier model where minority carriers would be either repelled, according to the former, or attracted by the interface potential, as reported by the latter. Nonetheless, regardless of the considered model, it appears clear

\* Corresponding author.

E-mail address: [stechmann@mpie.de](mailto:stechmann@mpie.de) (G. Stechmann).

that grain boundaries are heavily altering the carrier mobility and, as such, the open circuit voltage of the cell.

The electronic activity of grain boundaries is expected to depend on their crystallographic and chemical character [14]. Crystallographically, these interfaces can be characterized by 5 rotational parameters, 3 for the lattice misorientation across the interface and 2 for the position of the boundary plane with respect to the crystal lattice [14]. In contrast to the frequent understanding that only the misorientation across a grain boundary influences the properties of the interface, the grain boundary plane actually also plays an important role [15]. This becomes most strongly evident at twin boundaries where the coherent interface (a {111} plane in CdTe) has a very low energy; the opposite is true for the incoherent one (e.g. on a {112} plane) [16,17]. The rotational parameters can be determined using electron backscatter diffraction (EBSD) in a scanning electron microscope (SEM). Regular two dimensional EBSD-based mapping of orientations (“orientation microscopy”) allows the classification of grain boundaries based on their misorientation. Furthermore, the boundary trace orientation delivers one additional parameter. A more comprehensive characterization is possible by focused ion beam/electron backscatter diffraction (FIB/EBSD) tomography (also referred to as 3-dimensional orientation microscopy or commonly 3D EBSD) which allows all five parameters to be determined. It also provides a direct insight into the grain boundary network spatial arrangement. The technique is based on the combination of successive 2D EBSD orientation mapping and serial sectioning of the sample using ion milling in grazing incidence [18]. The 3-dimensional microstructure is then reconstructed using dedicated software. An important benefit of this approach also lies in the possibility to probe the evolution of a relevant set of parameters (grain size, texture, grain boundary character distribution etc) through the whole thickness (around 4  $\mu\text{m}$ ) of the strongly microstructurally-anisotropic CdTe layers.

One of the main concerns regarding ion milling is the modification of the sample surface microstructure due to the incoming high-energy ions. FIB milling is indeed known to induce crystallographic damages in many semiconductor materials (for example, 30 keV milling of silicon samples using gallium ions does not provide useable EBSD patterns due to too deep amorphisation of the material [19], similar observations on non-metallic materials have been reported by Zaefferer et al. [18,20]) and can lead to ion implantation [21] or to the creation of a gallium contamination

layer which may modify the electronic properties of the sample. Furthermore, in semiconductor materials, Mayer et al. [22] reported that the amorphous layer, created after ion-assisted surface sputtering, is likely to be proportional to the energy of the incoming gallium ions, thus preventing its use in case of materials having low bonding energies. Nevertheless, an extensive study conducted by Rischau et al. [23] on ion-beam induced damage formation in CdTe thin films, emphasized that the high ionicity of the Cd–Te bonds facilitates recovery from such surface modifications, and makes then the CdTe lattice highly resistant to amorphization. These conclusions are in agreements with the results obtained in this paper, where amorphization of the absorber layer was never observed as a result of milling using gallium ions accelerated at 30 keV. Therefore, FIB techniques appear to be suitable in this case and can thus be combined with orientation microscopy to perform tomographic analyses.

CdTe absorber layers from CdTe/CdS solar cells may be grown in two different configurations (Fig. 1), the conventional superstrate configuration, and the substrate configuration, the latter being investigated in this work. Two of the main advantages of this configuration, compared to the superstrate one, are, on the one hand, the possibility to deposit on non-transparent and flexible substrates and, on the other hand, a better control of the p–n junction properties due to its particular stacking sequence, as detailed by Gretener et al. [24] and Williams et al. [4]. Independent from the chosen configuration, CdTe solar cells have to undergo a specific post-treatment, in order to achieve decent efficiencies, during which chlorine is diffused into the material. This step is usually performed by annealing the cell in presence of cadmium-chloride ( $\text{CdCl}_2$ ) [2] or, as it has been recently proposed, magnesium chloride ( $\text{MgCl}_2$ ) [25]. Despite being the subject of numerous studies, the real effects of this post-treatment are still not fully understood, especially in terms of microstructural evolution. This particular point will be discussed in Section 4.2.

In the present work, the texture and microstructure, including grain boundaries, of CdTe thin films deposited in substrate configuration by a low temperature process [24] were investigated using 3D-EBSD. Based on the obtained results, the critical steps governing the grain boundary network formation were identified and a coherent growth model was proposed. This will be the cornerstones of a future grain boundary engineering approach applied to the design of such cells. The influence of the deposition

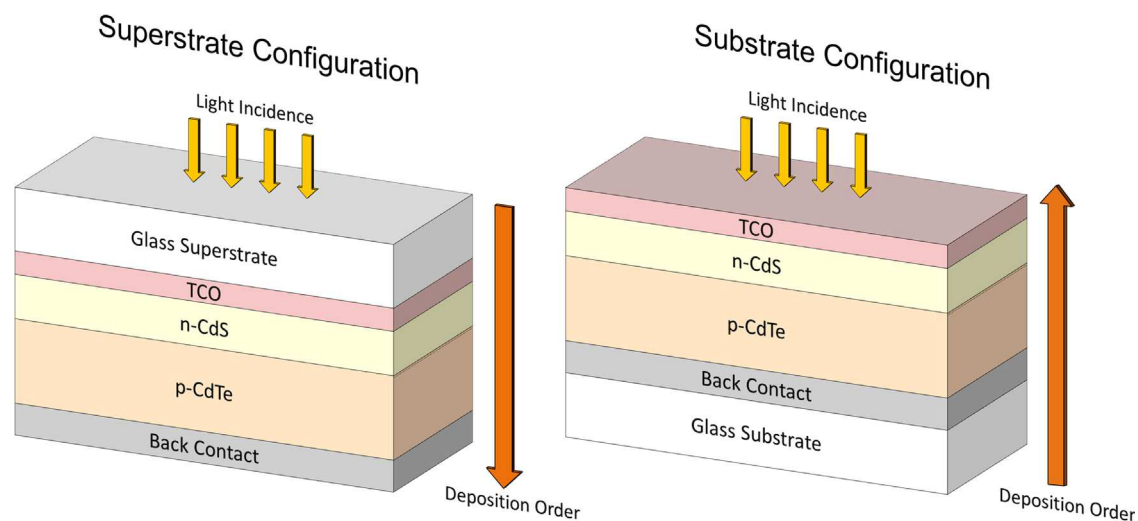


**Fig. 1.** CdTe/CdS solar cell grown in superstrate configuration (left) and substrate configuration (right). The glass substrate can be replaced by flexible and/or non-transparent substrates [24].

parameters will be discussed as well as the microstructural changes induced by the  $\text{CdCl}_2$  activation treatment.

## 2. Experimental procedure

The investigations were performed on two complete  $\text{CdCl}_2$ -annealed  $\text{CdTe}/\text{CdS}$  solar cells in substrate configuration, the first one deposited on a glass substrate and the second on a metallic molybdenum foil.<sup>1</sup> In addition, an as-deposited  $\text{CdTe}$  layer deposited on glass using the same conditions was also investigated to understand the influence of the annealing treatments on  $\text{CdTe}$  microstructure. Finally, a sample annealed without chlorine (later referred-to as simply-annealed) was studied as well to separate the effects of chlorine and heat treatment. All cells were produced at the Laboratory for Thin Films and Photovoltaics, EMPA Dübendorf in Switzerland using low-temperature processes, following the stacking sequence substrate/ $\text{Mo}/\text{MoOx}/\text{CdTe}/\text{CdS}/\text{ZnO}$  as described in [26]. They were all deposited at a substrate temperature of  $350^\circ\text{C}$  to a final thickness of approximately  $4\ \mu\text{m}$ . Only the two complete cells underwent two  $\text{CdCl}_2$ -annealing post-treatments. In both cases, the post-treatment was performed by depositing a  $\text{CdCl}_2$  layer on top of the stack (the first one occurring after the  $\text{CdTe}$  deposition step and the second after depositing the  $\text{CdS}$  layer), followed by an annealing step at  $435^\circ\text{C}$  for 25 min and  $360^\circ\text{C}$  for 25 min respectively in an oxygen-containing ambient. The layer annealed without chlorine underwent a single heat treatment under the same condition ( $435^\circ\text{C}$  for 25 min).

All samples were cut such that the cross section of the absorber layer was accessible at the edge of the sample. Then, in order to ensure good electrical conductivity and to minimize detrimental charging effects during SEM imaging, the non-conductive glass substrate was coated with silver paste. All pieces of information on the herein discussed samples are summarized in Table 1.

The SEM and EBSD investigations were performed using a Zeiss-Crossbeam XB 1540 FIB-SEM consisting of a Gemini field emission gun electron column and an Orsay Physics ion beam column mounted  $54^\circ$  from the vertical. For EBSD orientation mapping, an EDAX-TSL EBSD system with a Hikari camera was employed.

FIB-EBSD tomography was achieved by removing successive layers of material using gallium ion milling in grazing incidence at 30 keV acceleration voltage, a FIB working distance of 7.94 mm and an ion beam current of 500 pA. Two dimensional EBSD-orientation mapping was then performed on a free surface inclined  $70^\circ$  towards the primary beam. The electron acceleration voltage was 15 keV the working distance 13 mm and the electron probe current 10 nA. In order to allow automated data acquisition and serial sectioning, a fiducial marker was used to realign the images before and after each sequence by image recognition. The sample movement was performed according to the so-called “tilt setup” as has been detailed by Zaefferer et al. in [18],[27]. For each slice, three different areas were sequentially milled as depicted in Fig. 2. Two lateral surfaces were firstly milled to prevent shadowing effects from the neighboring material. The top surface was then sputtered in two steps: the first was a coarse milling, using a 2 nA beam current, aiming at removing material at the bottom of the milling field; this was followed by a smooth milling step with a 500 pA current, delimiting the area of interest on which the

**Table 1**  
Samples description.

Samples	Substrate	Post-treatments	Volume probed (3D EBSD)
2 Complete cells	Glass Mo	$2 \times \text{CdCl}_2$ -annealing ( $435^\circ\text{C} + 360^\circ\text{C}$ , 25 min)	$630\ \mu\text{m}^2 \times 3.5\ \mu\text{m}$ $760\ \mu\text{m}^2 \times 4\ \mu\text{m}$
As-deposited	Glass	N/A	$875\ \mu\text{m}^2 \times 3.5\ \mu\text{m}$
Simply-annealed	Glass	Single annealing, no Cl ( $435^\circ\text{C}$ , 25 min)	$950\ \mu\text{m}^2 \times 3.8\ \mu\text{m}$

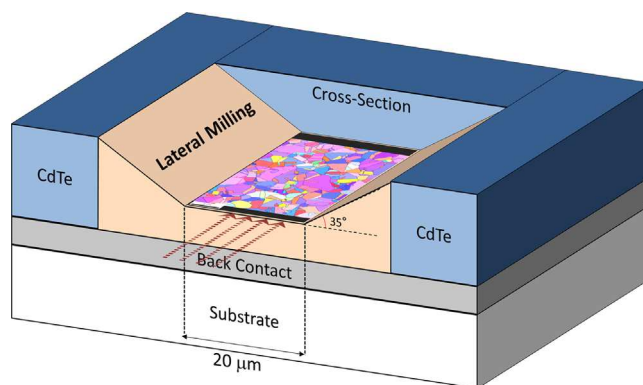


**Fig. 2.** Schematic of the FIB/EBSD tomography milling sequence. Red dashed arrows indicate the incoming gallium ions direction. (For interpretation of the references to color in this figure, the reader is referred to the web version of this article.)

**Table 2**  
Milling sequence parameters.

Objectives	FIB parameters	Milling time
TCO/CdS removal	2 nA/30 kV	once until CdTe layer is visible
Lateral milling	2 nA/30 kV	30 s for every slice
Rough surface milling	2 nA/30 kV	60 s for every slice
Fine milling for EBSD mapping	0.5 nA/30 kV	450 s for every slice

orientation mappings were performed. The FIB parameters for each step are summarized in Table 2. After each complete session, the beam was moved towards the surface to remove the next layer of material. In order to investigate the  $\text{CdTe}$  absorber layer, both the transparent conductive oxide (TCO) and the  $\text{CdS}$  layer (Fig. 1) had to be removed by FIB using a 2 nA, 30 keV accelerated  $\text{Ga}^+$  ion current. Once the absorber layer was exposed at the free surface, FIB-EBSD tomography was invoked. The orientation data were measured on a 3-dimensional cubic lattice with 70 nm step size in all 3 dimensions.

The collected EBSD orientation data were analyzed using EDAX-TSL OIM Analysis<sup>®</sup> version 6.2. All datasets were cleaned up first using grain confidence index (CI) standardization and then a grain dilation algorithm (single iteration). Both algorithms belong to the standard functions of the OIM Analysis software. Application of these functions guarantees that all accepted data points have good confidence for their orientation correctness. Furthermore, low-confidence data points directly on grain boundaries will be assigned to one or the other grain across the boundary in order to allow smooth grain boundary reconstruction. The 3D reconstruction and related pole figures were obtained using the in-house

<sup>1</sup> It is important to note that “deposited on glass”, respectively “on molybdenum”, only refers to the **substrate** composition. In both cases,  $\text{CdTe}$  is deposited on a  $\text{Mo}/\text{MoOx}$  back contact (see Fig. 1).



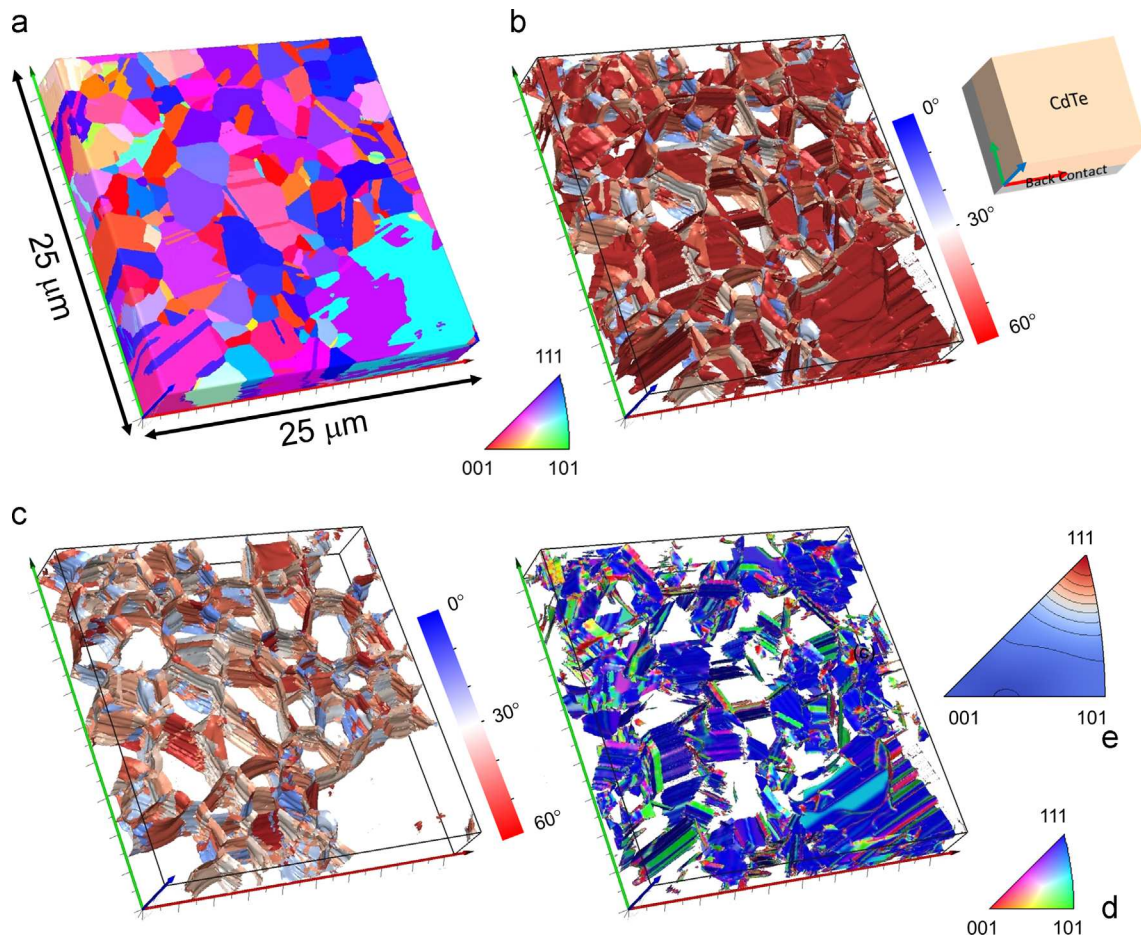


**Fig. 3.** Reconstructed grain boundary networks of the complete cell. (a) Grains colored for the crystallographic direction parallel to the growth direction, (b) the complete grain boundary network colored according to the disorientation angle, (c) only random high angle grain boundary network colored according to the disorientation angle, (d) only  $\Sigma 3$  twin boundary network colored according to the boundary plane crystallographic components (blue color denotes twin boundary developing on a  $\{111\}$  plane) and (e) corresponding boundary plane inverse pole figure indicating that twin boundaries are mostly developing on  $\{111\}$  planes (maximum intensity  $\sim 1000$  MRD). (For interpretation of the references to color in this figure, the reader is referred to the web version of this article.)

developed post-processing software QUBE<sup>2</sup> version 1.2.0.1 [28]. This is performed based on the voxelized structure resulting from the stacking of consecutive EBSD datasets. The voxel structure which is then substituted by a tetrahedra-based mesh along large angle grain boundaries, allowing a misorientation angle of at least  $5^\circ$ . This mesh is then refined using a Laplacian smoothing algorithm [28], enabling the crystallographic analysis of three dimensional grain boundaries. In the following, the “reconstructed” grain boundary network refers to the meshed interfaces network.

Once grain boundaries are meshed the software QUBE may return all their 5 rotational parameters, i.e. the angle and axis of misorientation and the crystallographic grain boundary surface normal. In cases of special boundaries, the misorientation will not be described as axis-angle pair but by means of the coincidence site lattice (CSL) model, which describes how many coincident atomic sites are formed between two misoriented crystals. The inverse of the fraction of coincidence points over all lattice points is expressed by the  $\Sigma$ -value. Twins are described by  $\Sigma=3$  or alternative by a  $60^\circ$  rotation about the  $\langle 111 \rangle$  axis. Other special boundaries considered in this paper are  $\Sigma=5$  ( $36.9^\circ \langle 100 \rangle$ ),  $\Sigma=7$  ( $38.2^\circ \langle 111 \rangle$ ), and  $\Sigma=9$  ( $38.9^\circ \langle 110 \rangle$ ).

Due to sample charging, significant misalignment and distortions are expected between successive measurements. The

misalignments were corrected by realigning all collected datasets prior to 3D reconstruction using the algorithm provided by EDAX-TSL OIM Analysis<sup>®</sup> and a manual realignment graphical user interface specifically developed at this aim. Nevertheless, the map distortions cannot be corrected yet and are, thus, responsible for small reconstruction artifacts.

For statistical comparison and texture measurement at the mesoscale ( $\sim 2000$  grains), several large-area 2-dimensional EBSD scans were performed on each sample at the two critical interfaces (p–n junction interface and back contact interface). These measurements were carried out using the same conditions as those above-mentioned for the 3D EBSD scans. A comparison between these large data sets and the smaller ones (about 300 grains each) from the 3D measurements shows that the later are still a reasonably good representation of the material in terms of texture and grain sizes.

Crystallographic textures were calculated using spherical harmonics expansion with an expansion coefficient of 34 and a Gaussian spread of  $5^\circ$ . All pertinent texture components are fiber textures with a fiber axis parallel to the deposition direction (z-direction). This is typical for thin films grown on amorphous substrate, where no sharp in-plane texture is observed [29]. Therefore, only inverse pole figures for the crystal directions in z-direction of the film are presented in the following discussion.

<sup>2</sup> QUBE now commercially available through Bruker Nano.

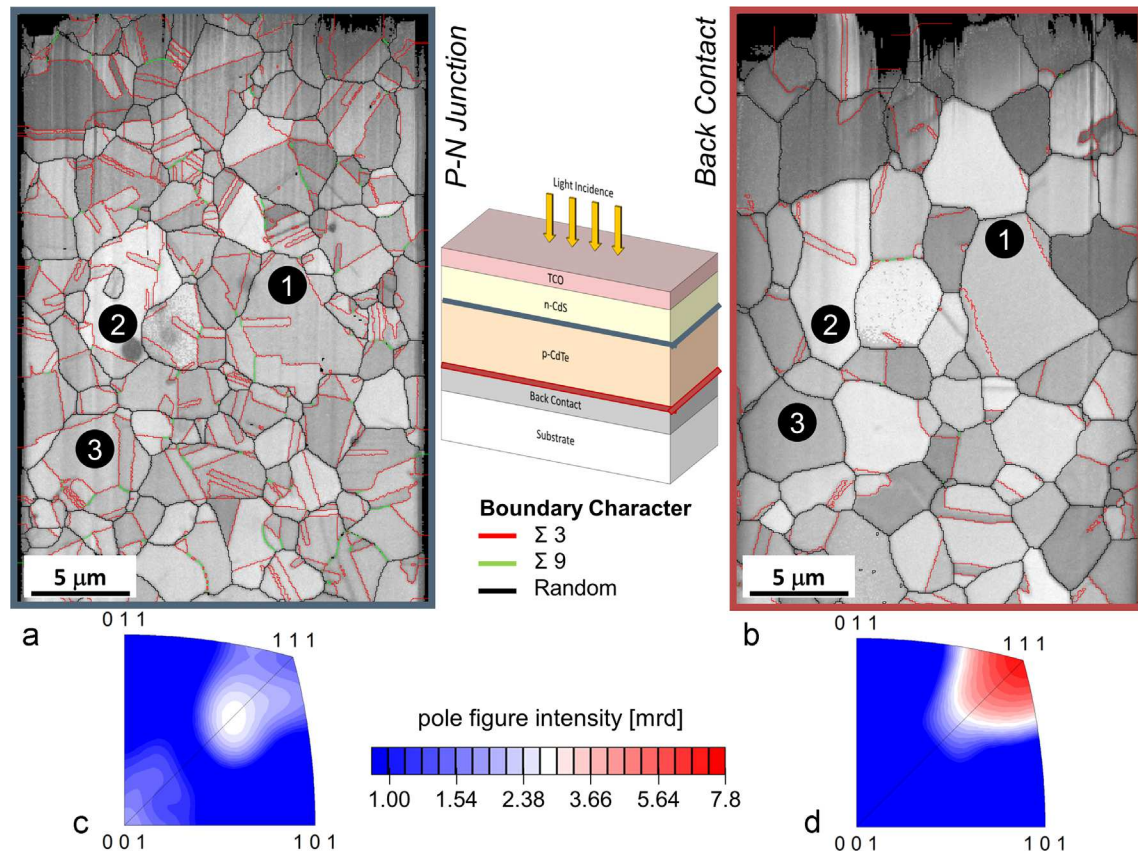


**Fig. 4.** (a) Image quality maps (top surface view) of the p–n junction interface and (b) of the back contact interface of the fully annealed structure. Grain boundaries are color-coded according to their rotational parameters. Same grains present at the two different interfaces are marked to evaluate their evolution more easily. [001] Inverse pole figures, displayed below, are based on mesoscale texture measurements ( $\sim 1700$  grains).

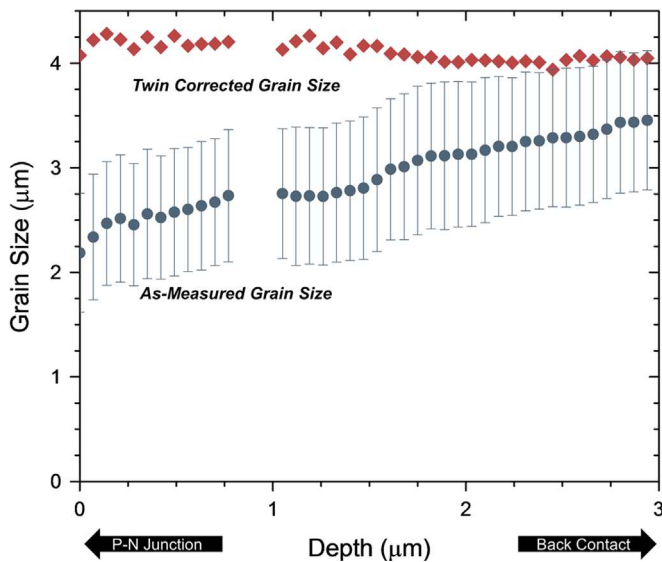


**Fig. 5.** Complete cell as-measured in-plane grain size (blue circles) and twin-corrected grain size (red rhombi) evolutions across the film thickness. Linear trend-line slope of the as-measured grain size is 0.376, intercept is 2.36  $\mu\text{m}$  and  $R^2$  is 0.9715. (For interpretation of the references to color in this figure, the reader is referred to the web version of this article.)

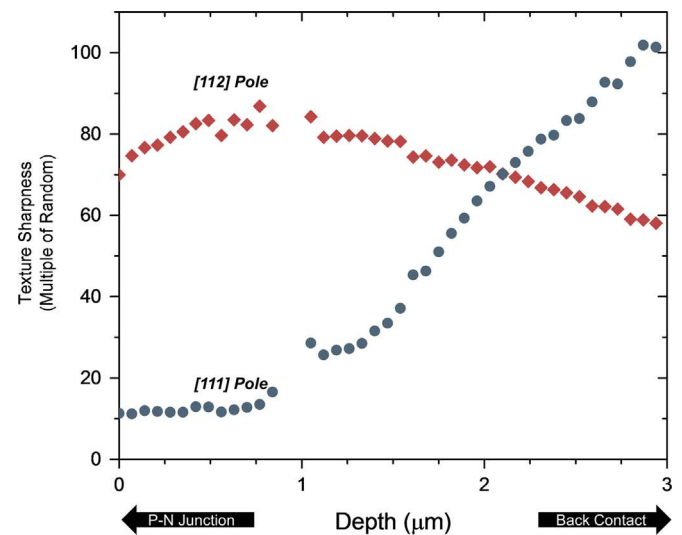


**Fig. 6.** Evolution of the {111} (blue circles) and {112} (red rhombi) texture components sharpness across the film thickness (complete cell). Texture sharpness is calculated with a  $5^\circ$  tolerance about the relevant crystallographic axis. (For interpretation of the references to color in this figure, the reader is referred to the web version of this article.)

### 3. Results

In the present work two substrates were used for deposition, glass and Mo foil. The Mo substrate was particularly interesting for

the experimental investigations, as it significantly reduces charging during 3D electron microscopy investigations, thus decreasing the amount of realignment required for a proper 3D reconstruction.

**Table 3**

Averaged grain boundary character distribution at the layers interfaces (complete cells). Arrows indicate the evolution from back contact to p-n junction

Boundary Type	Back Contact		P-N Junction
<b>Low Angle Boundaries (<math>&lt; 15^\circ</math>)</b>	6.9%		2.1%
<b><math>\Sigma 3</math>, 5, 7 and 9</b>	29.5%		61 %
<b><math>\Sigma 3</math> only</b>	25.5%		56.4 %
<b>Random High Angle Boundaries</b>	63.6%		36.9 %
<b>Total Boundary Length</b>	4 mm		4.6 mm

### 3.1. Complete, $\text{CdCl}_2$ -annealed cell

As presented in the reconstructed grain boundary networks in Fig. 3(b) and (c), the microstructure consists of columnar grains, enveloped by random high angle grain boundaries and standing perpendicular to both the substrate and p–n junction. The columnar grains are intersected by first order twin boundaries as shown in Fig. 3(b) and (d). Their density increases towards the p–n junction as it can be clearly observed in the image quality maps<sup>3</sup> presented in Fig. 4(a) and (b) and as it will be shown later in Fig. 7. Such a specific microstructure can also be described in terms of columnar twin related domains (TRD), the crystallographic description of which has been the subject of extended works [30].

The microstructures observed at the top and bottom of the absorber layer exhibit manifest disparities in many regards. Firstly, the in-plane grain size is about 35% smaller at the p–n junction interface than at the back contact (around  $2.44\ \mu\text{m}$  at the p–n junction, averaged over 1600 grains and  $3.28\ \mu\text{m}$  at the back contact, averaged over 1900 grains). From the tomography data, the evolution of the in-plane grain size can be expressed as a function of the depth across the layer thickness as plotted in Fig. 5. An almost linear evolution of this parameter, decreasing in the growth direction, is observed. In contrast, the twin corrected grain size, that is, the grain size measured if the  $\Sigma 3$ -misoriented grain boundaries (i.e. twin boundaries) are ignored when determining the grain boundary network, is depth-independent. This is a result of the previous statement that TRDs extend across the whole layer thickness.

The crystallographic texture of the material also strongly evolves along the deposition axis. At the p–n junction interface, as displayed in the inverse pole figure in Fig. 4(c), a slight  $\{112\}\parallel\text{GD}$  growth direction (GD) fiber texture, with an intensity of about 3 times of a random pole distribution (“mrd”=multiples of random distribution), is observed. Furthermore much weaker components close to  $\{111\}\parallel\text{GD}$  and  $\{127\}\parallel\text{GD}$  (which results from twinning from the  $\{111\}\parallel\text{GD}$  orientation as will be later shown and discussed in Fig. 12) are visible. Nevertheless, close to the back contact (i.e. where the deposition initially starts), the texture can be comprehensively described by a double fiber texture with a sharp  $\{111\}\parallel\text{GD}$  component (maximum observed sharpness being around 7.8 mrd) together with a much weaker  $\{112\}\parallel\text{GD}$  one (in the order of 3 mrd) as can be seen in Fig. 4(d) and in Table 4. The evolution of the intensities of the  $\{111\}\parallel\text{GD}$  and  $\{112\}\parallel\text{GD}$  fiber texture components across the layer are displayed in the pole plot presented in Fig. 6. The values used in this chart are obtained by integration over all pole figure intensities within the first  $5^\circ$  around its center. The graph emphasizes the strong decrease of the  $\{111\}$  pole intensity with increasing deposition thickness whereas the sharpness of the  $\{112\}\parallel\text{GD}$  component remains relatively stable over the whole film thickness.

In addition to grain size and texture analyses, the grain boundary character distribution (Table 3) can also be deduced from EBSD

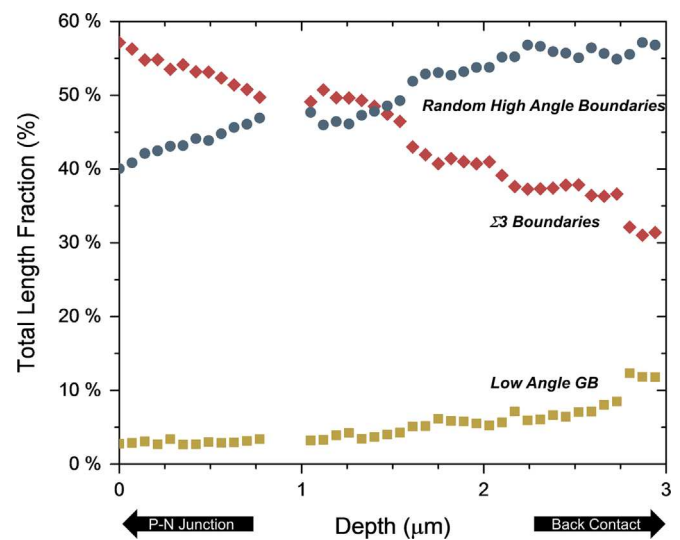


**Fig. 7.** Evolution of the low angle boundaries,  $\Sigma 3$  and high angle boundaries fraction across the film thickness (complete cell). The upper disorientation limit to define low angle boundaries is set to  $15^\circ$ .

measurements. The aforementioned microstructural and textural evolutions coincide with an increase of the first order twin boundaries fraction ( $\Sigma 3$ ) as depicted in Fig. 7. While its value is estimated at around 30% of the total grain boundary length at the back contact, it reaches up to 60% at the p–n junction. Such high amounts of twins were already reported in annealed-CdTe thin films [31,32]. In addition, the high percentage of  $\Sigma 9$  interfaces, reported in Table 3, is directly related to the widespread occurrence of  $\Sigma 3$  ones as their existence is geometrically enforced by successive twinning between adjacent grains (second-order twins).

From the 3D orientation datasets, the full five-parameter character of grain boundaries was determined. In the stereographic projection presented in Fig. 3(e), the density distribution of the crystallographic directions of the grain boundary normals is plotted for the  $\Sigma 3$  interfaces. The high density of boundary normals around the  $\{111\}$  direction indicates that most of them are coherent twins. Despite this observation, incoherent segments, including  $\{112\}/\{112\}$  and  $\{111\}/\{115\}$  boundary planes, with lengths up to  $2\ \mu\text{m}$  have also been observed. However, they represent only a marginal proportion of the total twin boundary network.

### 3.2. As-deposited CdTe absorber layer

The thin film in the as-deposited state was investigated in the same manner as the complete cells and its microstructure was found to be very different from the annealed one.

At the top surface, i.e. the position of the later p–n junction,<sup>4</sup> the microstructure consists of small  $\{111\}\parallel\text{GD}$  oriented columnar

<sup>3</sup> Image quality is calculated as the sum over the Hough peak intensities, which corresponds, roughly, to the total intensity of the Kikuchi bands in an EBSD pattern; the KAM value is calculated as the average over all misorientation angles calculated between the center pixel and all its neighboring pixels in a kernel.

<sup>4</sup> The as-deposited material does not have a p–n junction. Nevertheless, for consistency with the other samples we will refer to the area at the free surface of



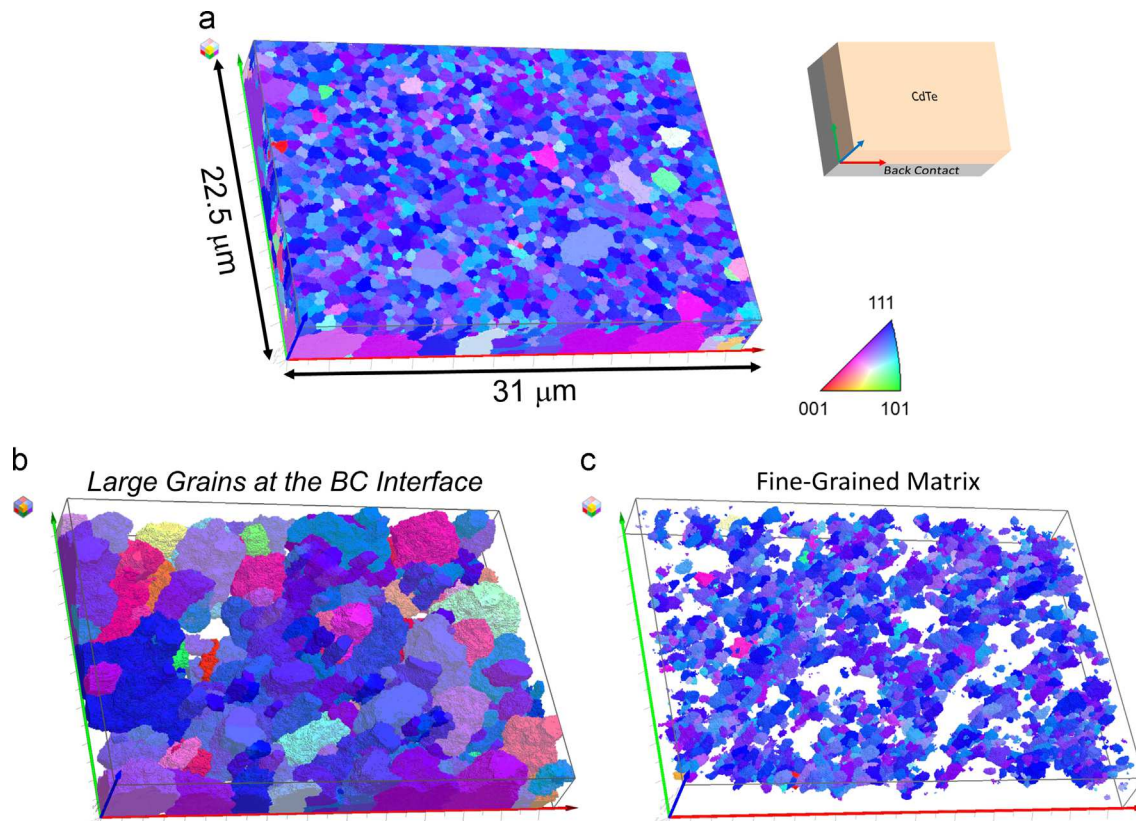


**Fig. 8.** (a) 3-Dimensionnall reconstruction of the as-deposited layer, (b) large grains developing from the back contact interface and (c) part of the fine-grained matrix present close to the p–n junction interface. Subset selection is based on the 3-dimensionnall volume of the grains; from 1 to 5000 voxels for the fine-grained matrix and above 5000 voxels for the large grains. Coloring is according to the crystal direction parallel to the deposition direction.

grains (later referred-to as fine-grained matrix), as visible in Figs. 8 (a) and 9(a), with an in-plane grain size in the order of  $0.75\ \mu\text{m}$  as already reported by several authors [24,32]. This value is 4 times smaller than grain diameters observed in the annealed material at the same position. Moreover, the acquired Kikuchi patterns are of poor quality, many of them consisting of the superimposition of two neighboring grain patterns. Indexation is thus delicate, resulting in the presence of the low confidence-index regions visible in Fig. 9(a).

In contrast, at the back contact interface, grains are significantly larger, in the order of  $3\ \mu\text{m}$  (Figs. 8(b) and 9(b)), which is comparable to the ones measured at the same location in the complete cells. In the core of the material, the grain size distribution is bimodal; the layer consisting of a combination of the two grain morphologies previously described (one example is given in Fig. 14 which will be later discussed). The transition between the two regimes is markedly visible in Fig. 10 where the depth dependence of grain size is plotted. While some big grains already reach the top surface, around 85% of the microstructure consists of the fine-grained matrix in the last  $2\ \mu\text{m}$  below the p–n junction.

A strong texture evolution is also concurrently observed along the growth direction, as depicted in Fig. 11. While the area close to the p–n junction exhibits an extremely sharp  $\{111\}$  fiber texture (see also Fig. 9(c)), the intensity of the  $\{111\}$  pole decreases with the distance to the back contact. An opposite trend is followed by the  $\{112\}$  pole intensity. At the back contact, the textures of the annealed and as-deposited samples show strong similarities. Both consist of a double  $\{111\}$ – $\{112\}$  fiber texture (Figs. 4

(d) and 9(d)) with comparable fractions of intensities. However, the total texture strength is higher in the complete cell. This will be later discussed in Section 4.2. All corresponding texture data are summarized in Table 4.

Grain morphologies and textures can be directly correlated by considering only the relevant fiber components, as shown in Fig. 12, resulting in the color-coded grain maps presented in Fig. 13. It is manifest that the fine-grained matrix is exclusively composed of  $\{111\}$  fiber oriented grains. Therefore, the decrease in texture sharpness is concurrent with the consumption of this matrix by the larger grains as visible in Fig. 11. In other words, the volume ratio of large grains to matrix grains, enforcing the grain size distribution, also governs the orientation spread. Furthermore, now only considering these thickest crystallites, it becomes apparent that only constituents of the  $\{112\}$  fiber (and their related twin components) exhibit a significant growth along the deposition axis. It has to be emphasized that the region labeled as "fine-grained matrix" in Figs. 10 and 11 contains a small number of large crystallites which strongly affect the texture due to their large in-plane area (Fig. 11) but are almost invisible in the grain size distribution (Fig. 10) due to their small number.

A further major difference between the as-deposited and annealed sample lies in the presence of a high number of low angle grain boundaries in the fine-grained matrix suggesting the presence of a high density of geometrically necessary dislocations. This observation is confirmed by the average value of the kernel average misorientation (KAM) which is directly proportional to the GND density [33] and a high fit value, as displayed in Fig. 14. The average KAM value is estimated to around  $0.75^\circ$  at the p–n junction surface, which is between three and four times higher than the values measured at the back contact interface. The detailed

(footnote continued)

this sample, which corresponds to the p–n junction of the annealed sample, as p–n junction.

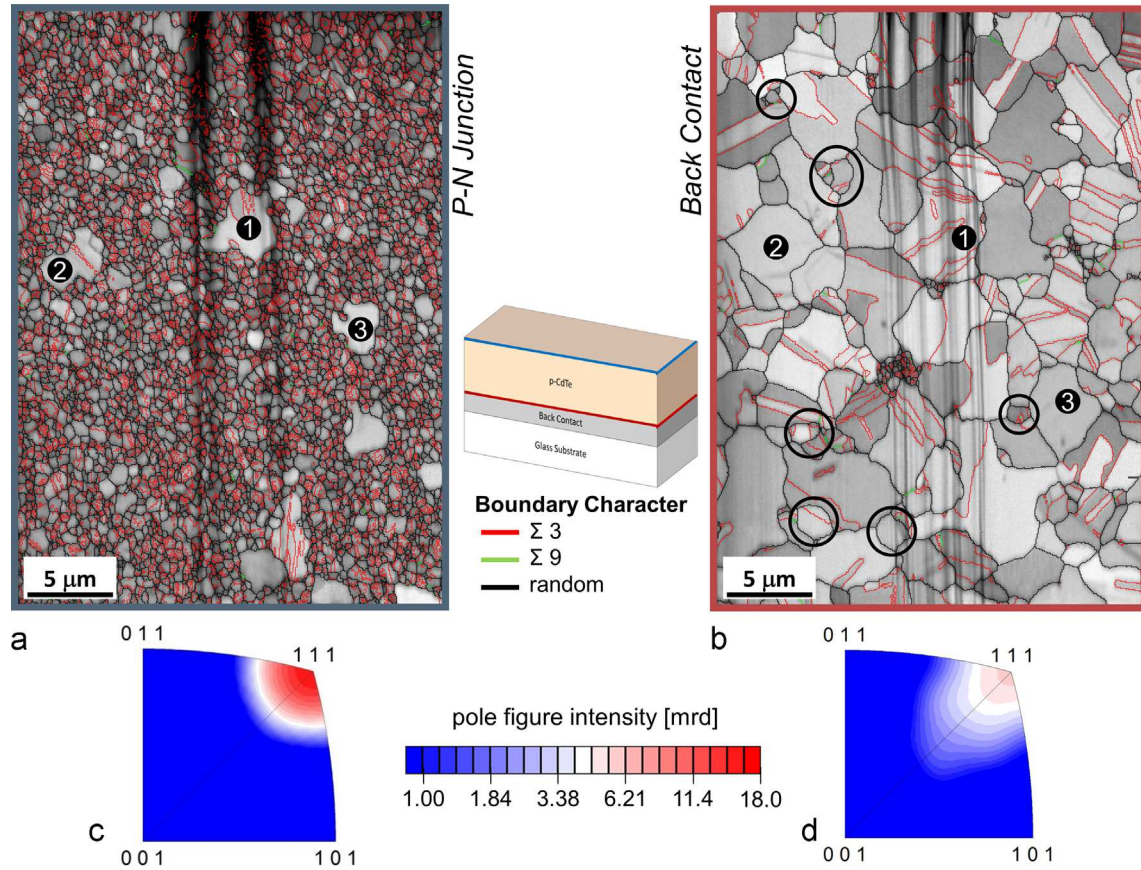


**Fig. 9.** (a) Image quality maps of the p–n junction interface (top surface view) and (b) the back contact interface of the as-deposited material. Grain boundaries are color-coded according to their rotational parameters. Same grains present at the two different interfaces are marked to facilitate the evaluation of their evolution. [001] Inverse pole figures, displayed below, are based on mesoscale texture measurements ( $\sim 3000$  and  $13,000$  grains respectively).

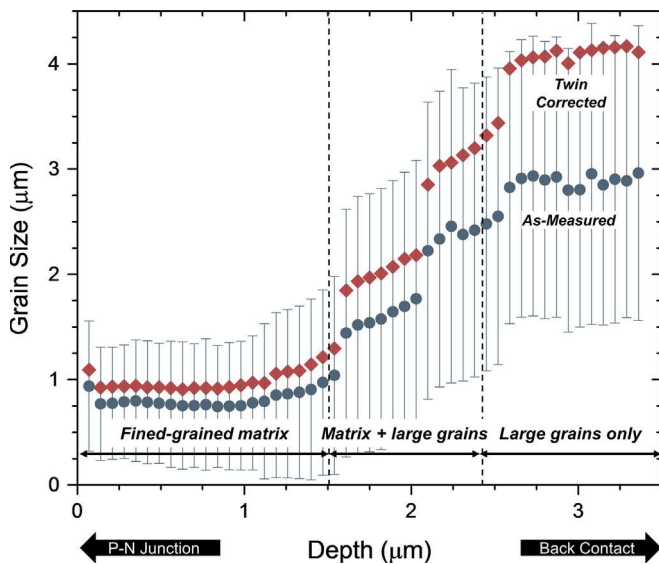


**Fig. 10.** As-deposited in-plane grain size (blue circles) and twin-corrected grain size (red rhombi) evolution across the film thickness. (For interpretation of the references to color in this figure, the reader is referred to the web version of this article.)

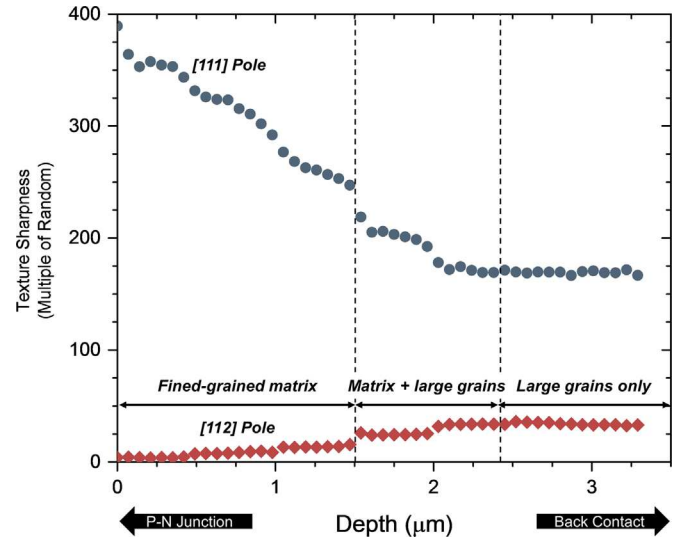


**Fig. 11.** Evolution of the {111} (blue circles) and {112} (red rhombi) texture components sharpness across the film thickness (as-deposited cell). Texture sharpness is calculated with a  $5^\circ$  tolerance about the relevant crystallographic axis. (For interpretation of the references to color in this figure, the reader is referred to the web version of this article.)

grain boundary character distribution evolution is presented in Table 5.

Finally, it is important to note here that there exists a third set of grains, encircled in Fig. 9(b), which is present only in the first

100–200 nm from the back contact interface. These grains are of intermediate size and neither belong to the {111} nor to the {112} fiber but rather exhibit random orientations. Moreover, their



relatively high image quality and low fit values indicate a low defect density which discriminate them from the rest of the matrix.

The texture and microstructure of the sample annealed without chlorine (“simply annealed”) represent an intermediate state between the as-deposited and the fully annealed sample. As noticeable in Fig. 13, the consumption of the highly textured fine-grained matrix by large crystallites still proceeds. The remaining bits of the  $\{111\}$ IGD small grains at the free surface are consequently only representing half of its total in-plane volume fraction.

## 4. Discussion

The absorber layer was deposited at a temperature of 350 °C. At the end of this deposition process the solar cell is not a working device yet and needs to undergo further heat treatments. We will first discuss the mechanisms active during the deposition step before addressing the structural changes promoted by the chlorine activation treatments.

**Table 4**  
Texture component intensities (multiples of random density). Data are taken from the inverse pole figures presented in Figs. 4 and 9.

Sample	Back contact		p–n junction	
	$\{111\}$	$\{112\}$	$\{111\}$	$\{112\}$
As deposited	~5	~3	~18	< 1
Simply-annealed	~4	~3	~10	~3
Complete cells	~8	~4	< 2	~3

### 4.1. Microstructure and texture evolution during deposition

#### 4.1.1. Grain morphology

At first sight, the microstructure of the as-deposited layer challenges general expectations: large grains are present at the position of nucleation (back contact interface) (Fig. 9(b)), while very small ones exist far away from the original seed layer (Fig. 9(a)), where growth would have been expected. This paradoxical observation can however be easily unraveled considering the fact that deposition occurs at a temperature of 350 °C; a regime where grain growth processes are already highly active. Consequently, the material which was deposited first (i.e. at the seed layer) had much longer time to undergo grain growth than the upper part of the layer, which was later deposited. Therefore, it may be assumed that the fine-grained microstructure present at the p–n junction is a depiction of the early deposition microstructural state. With increasing proximity to the back contact, the material has experienced longer annealing and grain growth, ultimately replacing the native grain arrangement. This statement is also supported by the presence of serrated grain boundaries (Fig. 9(b)) at the substrate interface suggesting that growth processes still proceed.

Additionally, the presence of small grains, with reduced defect density, very close to the substrate interface (encircled in Fig. 9(b)) may be indicative of a recrystallization nucleation event occurring simultaneously to deposition. This may occur by grain boundary bulging of existing crystallites due to the deformation built-in during material deposition. It is, nonetheless, delicate to assign these nuclei to pre-existing nucleation sites as the latter are ipso-facto replaced by the recrystallized microstructure and because twinning events tend to pseudo-randomize their orientations. However, it is a fact that this set of small grains neither belongs to the  $\{111\}$  fiber nor to the  $\{112\}$  one and only exists in the as-deposited layer (i.e. are later consumed by crystallites in their

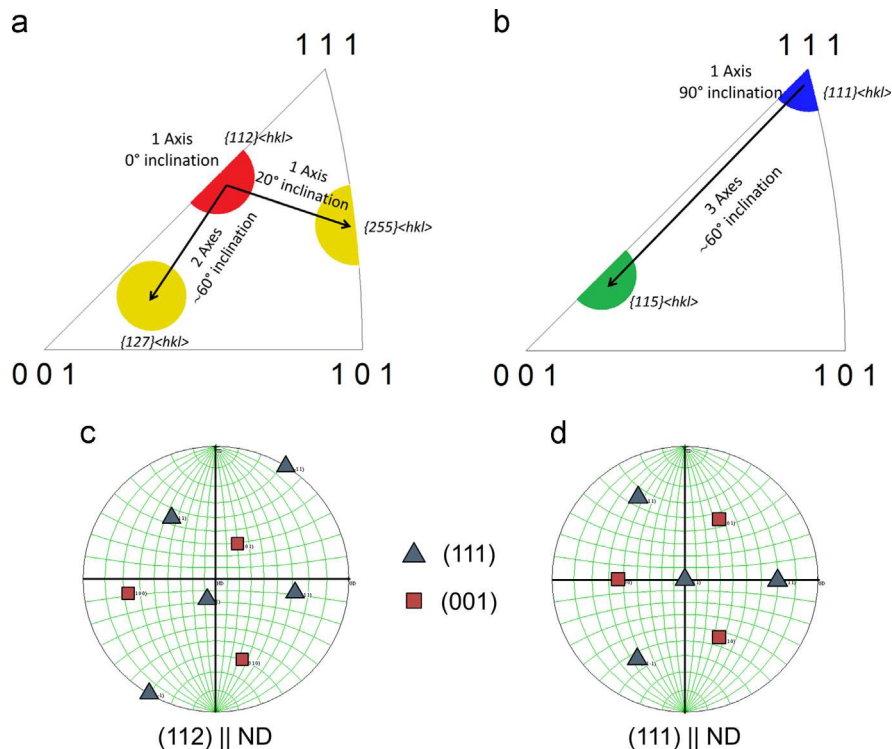


**Fig. 12.** Inverse pole figure taken along the growth direction displaying the crystal directions resulting from first order twinning from (a) a  $\{112\}$ ||ND and (b)  $\{111\}$ ||ND orientations. Poles are displayed with a 5° orientation spread. (c) and (d) display the  $\{111\}$  twinning planes and the  $\{100\}$  cube planes for (c) a typical  $\{112\}$ ||ND and (d) a typical  $\{111\}$ ||ND oriented grain. (For interpretation of the references to color in this figure, the reader is referred to the web version of this article.)

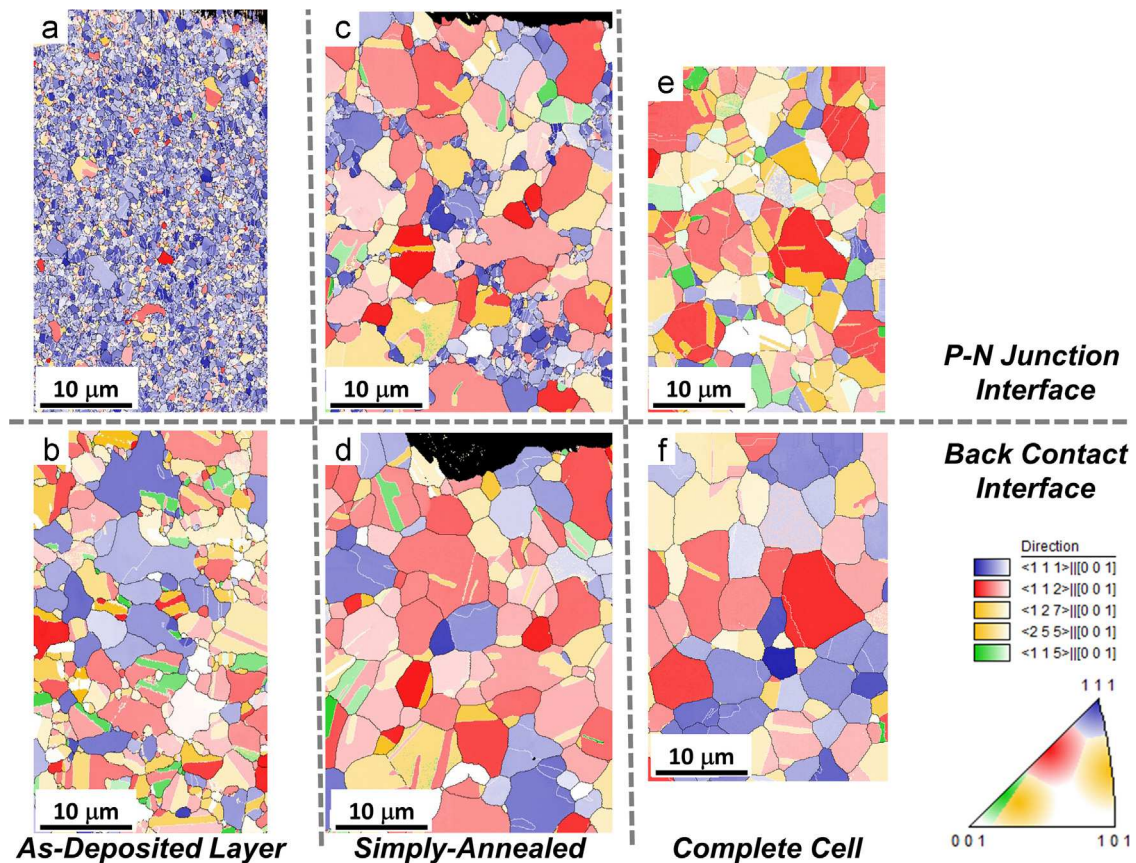


**Fig. 13.** Fiber-colored orientation maps at the extreme positions of each sample (upper part: p–n junction interface and bottom part: back contact interface). First column corresponds to the as-deposited layer, second column to the layer annealed without chlorine and last to the complete cell. Blue grains belong to the  $\{111\}$  fibers, red to the  $\{112\}$  and green and yellow are in twinning relationship with  $\{111\}$  and  $\{112\}$  respectively. Tolerated deviation angle is set to  $12^\circ$ . Grain boundaries are indicated by black lines and  $\Sigma 3$  boundaries by white lines. (For interpretation of the references to color in this figure, the reader is referred to the web version of this article.)

vicinity), emphasizing the clear orientation-dependence of the growth process which is discussed in the next part.

#### 4.1.2. Texture evolution

We first discuss the crystallographic origin of the different observed texture components, as they are displayed in Figs. 12 and 13.

During deposition, two independent texture components are formed, the  $\{111\}$ IGD fiber, marked in blue in Figs. 12 and 13, and the  $\{112\}$ IGD one, marked in red. The highest occurrence of the former can be inferred considering that  $\{111\}$  planes have the highest polarity and the highest atomic density in the sphalerite structure. As such, it is expected that  $\{111\}$ IGD-oriented grains constitute a good compromise between interface and surface energy minimization [29,34]. Similar  $\{111\}$ IGD as-deposited fiber textures have been frequently reported in the literature, independent of substrate and deposition configuration [35,36] (except for cases with epitaxial deposition). Besides these energy-arguments, the  $\langle 111 \rangle$  direction is also deposited at highest growth speed, probably because of the ease of construction of the dense  $\{111\}$  planes [35].

Less expected is the presence of  $\{112\}$ IGD grains. The appearance, admittedly sparse, of such grains in the fine-grained matrix suggests that this orientation also satisfies, in a lesser extent, the energetic requirements of deposition previously stated.

Besides these major fibers there exist 3 minor components which are in twinning relationship with the major ones, as indicated in Fig. 12. These are the  $\{115\}$ IGD component as a twin of from the  $\{111\}$ IGD fiber, and the  $\{127\}$ IGD as well as  $\{255\}$ IGD components as twins from the  $\{112\}$ IGD fiber. The  $\{127\}$ IGD is

created by twinning on one of the  $60^\circ$  inclined axes (see the pole figures Fig. 14 (c) and (d)) and the  $\{225\}$ IGD by twinning on the single  $20^\circ$  inclined axis.

The texture transition, from the very sharp  $\{111\}$ IGD texture of the matrix to the double fiber description observed at the back contact, can be comprehensively described in terms of growth with orientation selection. This is in support to the foregoing hypothesis suggesting that deposition and growth occur concurrently. Using 3D EBSD, it is indeed possible to compare the out-of-plane growth rate of constituents of different fibers. It then appears that  $\{112\}$ IGD oriented grains and their twins develop much faster than  $\{111\}$ IGD ones. This is distinctly visible in Fig. 13 (a) and (c), where some  $\{112\}$ IGD oriented grains are already found to extend across the whole layer thickness, and to exhibit significant lateral sizes, by the end of deposition. This observation suggests that the kinetic and energetic parameters, promoting the  $\{111\}$ IGD texture during the thickening of the layer, change in the growth stage, leading to a faster growth of the  $\{112\}$ IGD component. Zoppi et al. [35] proposed that this is due to the presence of fast-growing Te-terminated planes perpendicular to the substrate in  $\{112\}$ IGD oriented grains. Nevertheless, this would result in the formation of anisotropically-shaped crystallites and would also promote the growth of  $\{110\}$ IGD grains. Both of these features are not observed experimentally.

It is in fact not clear why grains from the  $\{112\}$ IGD fiber overgrow their neighborhood or, in other words, why the  $\{111\}$ IGD orientation is not favored anymore upon grain growth. Nevertheless, several hypotheses can be advanced:



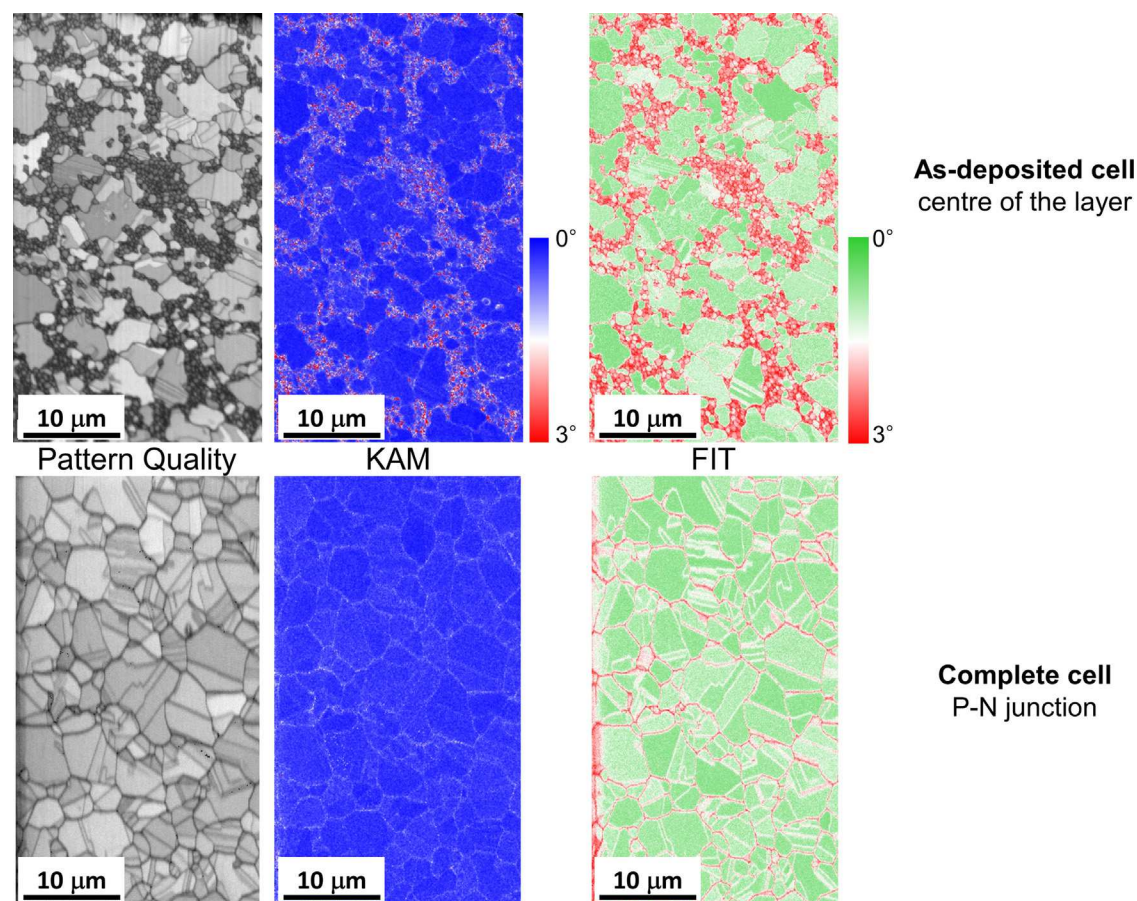


**Fig. 14.** EBSD-based measures of defect densities: Image quality, kernel average misorientation (1st neighbor) and fit map (linear color scales). Upper row: as-deposited cell, maps taken halfway between the back contact and p–n junction interfaces. The bimodal grain size distribution is clearly visible and the defective state of the fine-grained matrix as well (low confidence index, high KAM value and high fit value). Larger grains developing from the back contact appear with a much lower defect density. Lower row: fully-annealed cell close to back contact.

**Table 5**  
Averaged grain boundary character distribution at the absorber layer interfaces of the as-deposited cell. Arrows indicate the evolution from back contact to p–n junction

Boundary Type	Back Contact		P-N Junction
Low Angle Boundaries ( $< 15^\circ$ )	4.2%		13.2%
CSL Boundaries ( $\Sigma 3, 5, 7$ and $9$ )	47.2%		42.3%
CSL Boundaries ( $\Sigma 3$ only)	44.7%		40.5%
Random High Angle Boundaries	48.6%		44.5%
Total Boundary Length	5.5 mm		2 mm

- On the one hand,  $\{111\}$ IGD grains are subject to texture pinning since this is the main fiber component of the as-deposited state. When assuming  $15^\circ$  as the maximum misorientation for low-angle grain boundaries, which are supposed to have reduced growth mobility, 25% of the encounters between two  $\{111\}$ IGD-oriented grains will result in the formation of such an interface. In contrast,  $\{112\}$ IGD oriented grains will never form a low-angle grain boundary with grains from the  $\{111\}$ IGD fiber.
- The initial as-deposited microstructure may exclusively be  $\{111\}$ IGD textured because of both surface and substrate interface energy minimization. At the back contact interface, however, where growth starts, only the substrate interface energy has to be taken into account since the grains do not exhibit free surfaces anymore. Therefore, it can be envisaged

that the  $\{112\}$ IGD orientation minimize this parameter despite having a higher surface energy which would prevent them from massively nucleating in the early stage of deposition. This energetic difference might be due to the polarity difference between the highly polar  $\{111\}$  planes and non-polar  $\{112\}$  ones [37]. Moreover, it is known that (111) A Cd planes and (111) B Te planes have different interface energies due to their dissimilar chemical compositions [38] leading to a higher growth rate of the A-type planes. If the above assumption is true, the observed abnormal growth could be polarity-selective, which we cannot check, however.

- $\{111\}$ IGD and  $\{112\}$ IGD grains do not accommodate elastic strain in the same way because of the anisotropy of the different effective biaxial moduli of CdTe (CdTe Zener anisotropic factor is 2.1 [39,40]). As such, the strain energy density developing at the



substrate interface is higher in {111}||GD grains which would in turn favor their consumption [29].

- Finally, as the {111}||GD grains grow quicker during deposition they seem to accumulate more growth defects, most probably stacking faults, as compared to their {112}||GD counterparts. As a consequence, there is a higher driving force for {112}||GD grains consuming {111}||GD grains than vice versa.

#### 4.1.3. Growth model

The microstructural evolution observed during the deposition step can be caused by three distinct processes [41]. The first is primary recrystallization (RX), which requires the nucleation of new grains, whose growth is then driven by the consumption of grain-internal defects (mainly dislocations); the second is normal grain growth (NGG), which proceeds by homogeneous growth of already existing and mainly defect-free crystals, the driving force being the grain boundary energy; and finally abnormal grain growth (AGG), also referred to as secondary recrystallization, which proceeds, after a nucleation stage, by growth of only few, well-selected grains out of a matrix of already defect-free grains. In the last case, the selection process (which is a kind of a nucleation process) is in many cases unclear. It may be due to grain-internal defects, but also due to special grain boundary properties. The driving force is, as is in the case of NGG, the energy stored in the grain boundaries.

The bimodal grain size distribution and the strong microstructural change between the two relevant interfaces, observed in the thin film, exclude the possibility of normal grain growth. Nevertheless, it is not straight-forward to make the distinction between primary and secondary recrystallization. Indeed, on the one hand, the as-deposited grains show a high amount of grain-internal defects, as pointed out by all defect indicators obtained by EBSD, i.e. low image quality, high value of the kernel average misorientation (KAM) and high fit value (Fig. 14).<sup>5</sup> On the other hand, the consumed matrix is composed of a high number of very small grains and, as such, exhibits a substantial boundary density. Therefore, both phenomena can be reasonably expected and only an estimation of the driving force intensity can discriminate between the two.

In the case of primary recrystallization, the driving force is given by the stored dislocation energy as displayed in Eq. (1) [41]:

$$P_{RX} = 0.5 \times \rho G b^2 \quad (1)$$

where  $\rho$  is the dislocation density released during recrystallization,  $G$  is the shear modulus and  $b$  the norm of the dislocation's Burgers vector ( $a/2 \langle 110 \rangle$  for face-centered cubic materials with  $a=648$  pm the lattice constant of CdTe). Based on the data reported in [40,42,43], the shear modulus of CdTe can be averaged at 11.7 GPa. The average dislocation density is estimated using the KAM parameter obtained by EBSD. Indeed, according to Konijnenberg et al. [33] this value is directly proportional (under some assumptions) to the geometrically necessary dislocations (GND) density as expressed in Eq. (2):

$$\rho = (c/(ba)) \times \text{KAM} \quad (2)$$

where  $b$  is the norm of the Burgers vector,  $a$  is the step size of the measurement and  $c$  is a constant in the order of 3–5. In order to obtain proper KAM values the effect of orientation noise in the measurement has to be taken into account. Therefore, the parameter used in Eq. (2) is in fact the difference between the average KAM value in the defected matrix and the one in well-recrystallized grains. From statistical analysis of the data

obtained by EBSD, average GND densities of  $7.6 \times 10^{14} \text{ m}^{-2}$  and  $1.14 \times 10^{14} \text{ m}^{-2}$  are estimated in the fine-grained matrix and in the larger grains respectively. According to Eq. (1), this corresponds to a driving force for primary recrystallization of 0.8 MPa.

Correspondingly, the driving force for secondary recrystallization is given by the energy of the consumed boundaries which can be approximated by Eq. (3) [41]:

$$p_{AGG} = 3\gamma/d \quad (3)$$

Where  $\gamma$  is the grain boundary energy and  $d$  the grain size of the consumed matrix (here taken to be  $0.75 \mu\text{m}$ ). The average grain boundary energy is set to  $1 \text{ J/m}^2$  by overestimating the value of  $0.8 \text{ J/m}^2$  obtained by density functional theory (DFT) calculation by Park et al. [17] in the case of a symmetric  $\Sigma 5$  boundary in unfavorable Cd-rich environment. This provides an estimated driving force for abnormal grain growth of about 4 MPa.

As shown by the calculations above, the driving force stored in form of grain boundary energy is five times higher than the one corresponding to the dislocation-stored energy. It is, however, very likely that both stored energies contribute to the growth process since both pressures are in the same order of magnitude. Indeed, the nucleation event cannot be uniquely pinpointed; it may be a subgrain growth process of {112}||GD oriented grains, as suggested by the presence of the small grains close to the back contact interface.

In any case, the microstructure development should be addressed as a mixed primary recrystallization-abnormal grain growth process which is, however, dominated by the latter one.

The above discussion may be summarized as follows:

1. During deposition small {111}||GD and {112}||GD oriented grains nucleate on the substrate with a number ratio varying between 5/1 and 10/1. These grains grow as thin columns ( $0.5 \mu\text{m}$  diameter with length equal to the film thickness) during the thickening of the film.
2. Due to the high substrate temperature, a concomitant recrystallization process is triggered at the back contact interface due to the high driving forces stored in grain boundaries and in crystallographic defects.
3. The growth of the grains into the fine-grained as-deposited matrix is highly orientation-dependent resulting in a change of texture fraction of the {111}||GD to {112}||GD components from  $400/10=40$  to  $175/30=5.8$  (displayed in Fig. 11). In addition to the texture change, the grains grow to a diameter about 5 times larger than the original grain size at the free surface.
4. Recrystallization proceeds rapidly in deposition direction, leading to an as-deposited layer where the first two microns close to the back contact are already recrystallized and where some of the {112}||GD-oriented grains already extend through the whole film thickness.

#### 4.2. Microstructure and texture evolution during annealing and role of chlorine

Once deposition was completed, the material was annealed two further times at two different temperatures, both higher than the initial deposition temperature, in the presence of  $\text{CdCl}_2$ . In the following section we will discuss the microstructural and textural evolution during these annealing processes but also the role of chlorine. For this, one sample was annealed without chlorine and its microstructural changes are compared to that of the other samples.

The cell annealed without chlorine represents an intermediate state between the as-deposited cell and the complete one. After only a simple annealing, recrystallization is still incomplete and some vestiges of the fine-grained matrix are still observed at the

<sup>5</sup> The fit value is the angular deviation between the measured Kikuchi band positions and the recalculated one after orientation determination.

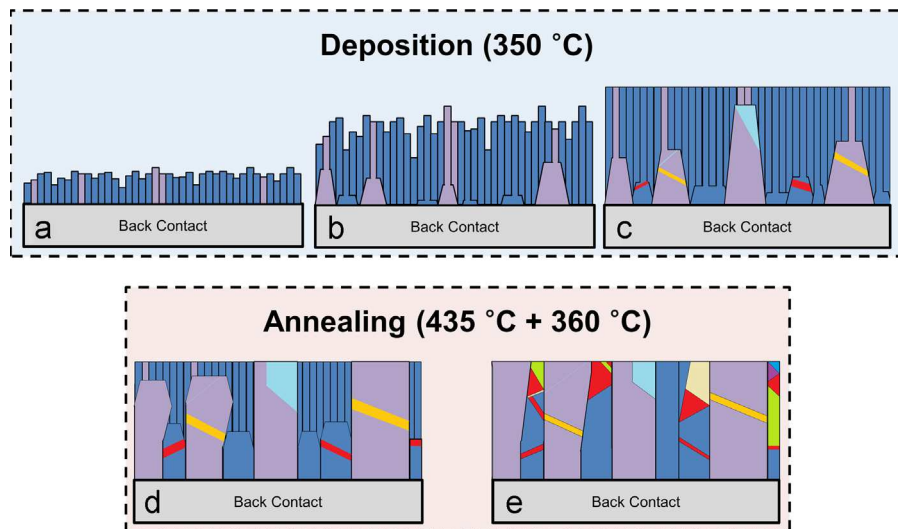


**Fig. 15.** Cross-section schematic displaying grain size and texture evolution during the deposition (top row) and during the annealing post-treatments (bottom row). Grains are color-coded according to their orientation relative to the deposition direction.

free surface. Nevertheless, grain boundaries are no longer serrated suggesting that normal growth has taken place.

Moreover, it is apparent from the 3-dimensional data that grains present at the back contact continue to grow in a columnar manner while intense twinning takes place in their interior. Therefore, the decrease in in-plane grain size observed along the growth direction is only due to twinning and not to the formation of new crystallites. The twin-corrected grain size is thus constant through the whole film thickness (Fig. 5) and a clear honeycomb structure appears in the 3-dimensionnal reconstruction of the random high angle grain boundary network (Fig. 3).

A notable difference between the microstructures observed at the back contact interface before and after annealing lies in the grain boundary character distribution. Indeed, the relative amount of twin boundaries present there is decreasing from 45% in the as-deposited material to 40% in the simply-annealed material. It is also worth mentioning that this trend is perpetuated, in an even more drastic way, in the complete cell where only 26% of the boundaries present at the back contact interface are twins. Therefore, it can be expected that twin boundaries are annealed-out during normal grain growth following the initial recrystallization step. Indeed, this process is much slower and leads, probably by movement of incoherent segments or by thermal motion of dissociated dislocations, to the disappearance of the in-grain twins (Fig. 13b,d,f) as suggested by Wang et al. in the case of FCC metals [44].

It is likely that chlorine may play a role therein by affecting the grain boundary mobility, as suggested by Consonni and Feuillet [45]. Nonetheless, more data are required to clearly discriminate the role of chlorine in this mechanism.

Finally, it should be stressed from the previous discussion that chlorine does not trigger recrystallization since the same phenomenon is observed in the simply-annealed layer which has not been exposed to chlorine. Upon further annealing treatments, as undergone by the complete cell during copper doping and further layer depositions, it is very likely that the recrystallization of the simply annealed layer would be completed. This would finally most likely lead to the same microstructure as observed in the complete cell annealed with chlorine, since the recrystallizing front has the same texture, grain size and grain boundary character distribution as the grains observed at the p–n junction of the complete cell.

#### 4.3. Understanding the complete cell microstructure: further annealing and growth model

The complete cell, i.e. after two annealing in presence of chlorine, microstructure can be apprehended as the result of the continuation of the previously-described mechanisms.

As aforementioned, grain boundaries at the back contact become smooth as a result of normal grain growth following recrystallization. In addition, the annealing-out of twin boundaries appears more clearly than in the simply-annealed material since only a quarter of the total grain boundaries are  $\Sigma 3$  interfaces. Finally, the as-deposited fine-grained matrix is now completely consumed, leaving behind TRDs extending across the whole layer thickness, as depicted in the 3D reconstruction in Fig. 3(a) and (c), with an in-plane grain size of around 4  $\mu\text{m}$ .

In order to understand the texture evolution during the final annealing steps, two facts have to be pointed out: first, the starting microstructure before annealing, as displayed schematically in Fig. 15 (c), consists of large columnar grains, traversing the whole film thickness and mainly belonging to the {112} fiber. These grains show a number of annealing twins created during the growth parallel to deposition as indicated in Fig. 15(a) and (b). They are embedded in a matrix of small, columnar, as-deposited grains belonging to the {111} fiber. The second thing to point out is that the first annealing step occurs at a significantly higher temperature as the deposition. All growth processes are therefore enhanced.

During the annealing two processes proceed: the first process concerns the already fully developed columnar {112}||GD grains. They undergo some minor grain growth, leading to more straight enveloping large angle grain boundaries. More importantly, part of the twins inside of these columnar grains disappears, probably by the movement of incoherent grain boundary segments. As a result the texture of these grains becomes sharper, see Fig. 4(c). The second process concerns the only slightly grown grains belonging to the {111} fiber. These grains now grow with a larger growth rate in deposition direction. It is well known that high growth rates implicate a high amount of twinning caused by growth accidents. These grains therefore develop a high amount of twins at the p–n junction as is seen Fig. 4(a) and displayed schematically in Fig. 15 (e). The sharpness of the {111} fiber close to the p–n junction therefore decreases due to the twinning chains, as is visible in Fig. 4(c).

The above discussion may be summarized as follows (see also Fig. 15):

1. During annealing, the recrystallization triggered during deposition continues. Due to the growth advantage of the {112} $\parallel$ GD-oriented grains, most of them have already developed through the whole layer after the first annealing, which is not the case for their {111} $\parallel$ GD-oriented counterparts. Moreover, the annealing-out of twins is observed at the back contact, resulting in an interface where the total length of twin boundaries is halved after the complete CdCl<sub>2</sub> annealing. This can be either due to the presence of chlorine or occurring during the second annealing.
2. Since temperature is significantly higher during annealing than during deposition (435 °C/350 °C) the growth rate and, thus, the twinning rate is enhanced for those grains which are not yet completely grown, i.e. mainly grains from the former {111} fiber component. This explains the fact that {112} $\parallel$ GD-oriented grains are less prone to twinning than {111} $\parallel$ GD-oriented ones. It also explains the higher occurrence of twin boundaries at the p–n junction in the complete cell, whose total length is approximately doubled in comparison with the microstructure present at the back contact interface.
3. Recrystallization ends when the originally defected layer is completely consumed, leaving a weak {112} texture together with components associated with orientations in twinning relationship with {112}-fiber grains and {111}-fiber grains. The apparent reduction of grain size is, therefore, only due to the high amount of twin boundaries and not due to the formation of new grains during annealing.

## 5. Conclusion

Understanding the growth of CdTe thin film solar cells in substrate configuration was made possible by the use of FIB/EBSD tomography. It appears that recrystallization is already triggered before the end of the deposition step and still continues during a typical CdCl<sub>2</sub> annealing post-treatment. Our results suggest that:

1. CdCl<sub>2</sub> is de facto not responsible for recrystallization but is nevertheless likely to affect its kinetic due to its segregation at grain boundaries. This is in strong contrast with what has been proposed in the literature for cells grown in superstrate configuration, which is, as of the writing of this paper, the only source of detailed microstructural data.
2. In addition, driving force calculations emphasize the crucial role of grain boundary energy which contributes predominantly to the observed microstructural changes with respect to the lower stored-deformation energy.
3. The grain boundary network existing in the finally annealed material consists of columnar grains with random high angle boundaries. These grains are intersected by twin boundaries whose density increases closer to the p–n junction interface and thus form twin-related domains.
4. It is apparent that the final grain size, texture and grain boundary network strongly depend on the interplay of deposition and annealing parameters. During deposition the seed layer, from which columnar growth proceeds, is created while during annealing the columnar structure and its twin-content is finalized. By controlling the rate of growth during both processes, i.e. by adjustment of deposition temperature, deposition rate and amount of chlorine it should be possible to control the final microstructure, thus opening possibilities for grain boundary engineering approaches.

Due to the particular microstructure formation mechanisms aforementioned, process optimization guidelines may be proposed. Firstly, the CdS is deposited on a semi-recrystallized microstructure with variable roughness and epitaxial relationships depending on whether the underlying grains are already recrystallized or not. The strong microstructural evolution of the CdTe layer during the successive heat treatments is then likely to affect the metallurgical junction and may introduce significant stresses at this interface. In addition, diffusion of chlorine, copper and other electronically important trace elements is also likely to be affected by the particular grain boundary network observed in the as-deposited cell. Finally, the large grain size measured at the back contact, coupled with limited bulk diffusion of these elements and the absence of further recrystallization, may enforce a relatively low average doping concentration at this interface. The here presented understanding of the microstructure evolution in general and grain boundary network in particular, thus offers the potential for tailoring the grain boundary network through grain boundary or microstructure engineering, respectively.

## Acknowledgments

The authors are deeply grateful to Monika Nellesen and Katja Angenendt for the technical assistance supporting this work and to the Max Planck Society for funding this project.

## References

- [1] D. Bonnet, P. Meyers, Cadmium-telluride-material for thin film solar cells, *J. Mater. Res.* 13 (1998) 2740–2753 (accessed 07.01.14) (<http://www.scopus.com/scopus/inward/record.url?eid=2-s2.0-0032186945&partnerID=40&rel=R6.5.0>).
- [2] K. Durose, P.R. Edwards, D.P. Halliday, Materials aspects of CdTe/CdS solar cells, *J. Cryst. Growth* 197 (1999) 733–745 (accessed 07.01.14) (<http://www.science-direct.com/science/article/pii/S0022024898009622>).
- [3] D. Bonnet, Manufacturing of CSS CdTe solar cells, *Thin Solid Films* 361 (2000) 547–552, [http://dx.doi.org/10.1016/S0040-6090\(99\)00831-7](http://dx.doi.org/10.1016/S0040-6090(99)00831-7).
- [4] B.L. Williams, J.D. Major, L. Bowen, L. Phillips, G. Zoppi, I. Forbes, et al., Challenges and prospects for developing CdS/CdTe substrate solar cells on Mo foils, *Sol. Energy Mater. Sol. Cells* 124 (2014) 31–38, <http://dx.doi.org/10.1016/j.solmat.2014.01.017>.
- [5] J. Perrenoud, L. Kranz, C. Gretener, F. Pianezzi, S. Nishiwaki, S. Buecheler, et al., A comprehensive picture of Cu doping in CdTe solar cells, *J. Appl. Phys.* (2013), <http://dx.doi.org/10.1063/1.4828484>.
- [6] B.G. Mendis, L. Bowen, Q.Z. Jiang, A. Contactless, Method for measuring the recombination velocity of an individual grain boundary in thin-film photovoltaics, *Appl. Phys. Lett.* 97 (2010) 092112, <http://dx.doi.org/10.1063/1.3486482>.
- [7] I. Visoly-Fisher, S.R. Cohen, A. Ruzin, D. Cahen, How polycrystalline devices can outperform single-crystal ones: thin film CdTe/CdS solar cells, *Adv. Mater.* 16 (2004) 879–883, <http://dx.doi.org/10.1002/adma.200306624>.
- [8] L.M. Woods, G.Y. Robinson, D.H. Levi, The effects of CdCl<sub>2</sub> on CdTe electrical properties using a new theory for grain-boundary conduction, In: *Proceedings of the Conference Record of the Twenty-Eighth IEEE Photovoltaics Specialists Conference-2000* (Cat. No. 00CH37036), 2000, pp. 603–606, doi:10.1109/PVSC.2000.915914.
- [9] C. Li, Y. Wu, J. Poplawsky, T.J. Pennycook, N. Paudel, W. Yin, et al., Grain-boundary-enhanced carrier collection in CdTe solar cells, *Phys. Rev. Lett.* 112 (2014) 156103, <http://dx.doi.org/10.1103/PhysRevLett.112.156103>.
- [10] B.G. Mendis, K. Durose, Prospects for electron microscopy characterisation of solar cells: opportunities and challenges, *Ultramicroscopy* 119 (2012) 82–96, <http://dx.doi.org/10.1016/j.ultramic.2011.09.010>.
- [11] W.K. Metzger, D. Albin, M.J. Romero, P. Dippo, M. Young, CdCl<sub>2</sub> treatment, S diffusion, and recombination in polycrystalline CdTe, *J. Appl. Phys.* 99 (2006) 103703, <http://dx.doi.org/10.1063/1.2196127>.
- [12] S.A. Galloway, P.R. Edwards, K. Durose, Characterisation of thin film CdS/CdTe solar cells using electron and optical beam induced current, *Sol. Energy Mater. Sol. Cells* 57 (1999) 61–74 (accessed 07.01.14) (<http://www.sciencedirect.com/science/article/pii/S0927024898001688>).
- [13] K. Durose, D. Boyle, A. Abken, C.J. Ottley, P. Nolle, S. Degraeve, et al., Key aspects of CdTe/CdS solar cells, *Phys. Status Solidi B* 229 (2002) 1055–1064 (accessed 07.01.14) ([http://onlinelibrary.wiley.com/doi/10.1002/1521-3951\(200201\)229:2%3C1055::AID-PSSB1055%3E3.0.CO;2-W/abstract](http://onlinelibrary.wiley.com/doi/10.1002/1521-3951(200201)229:2%3C1055::AID-PSSB1055%3E3.0.CO;2-W/abstract)).



- [14] L. Priester, Grain Boundaries, Springer Netherlands, Dordrecht (2013) <http://dx.doi.org/10.1007/978-94-007-4969-6>.
- [15] J. Chen, T. Sekiguchi, D. Yang, Electron-beam-induced current study of grain boundaries in multicrystalline Si, *Phys. Status Solidi C* 4 (2007) 2908–2917, <http://dx.doi.org/10.1002/pssc.200675435>.
- [16] D. Wolf, Correlation between structure, energy, and ideal cleavage fracture for symmetrical grain boundaries in fcc metals, *J. Mater. Res.* 5 (1990) 1708–1730, <http://dx.doi.org/10.1557/JMR.1990.1708>.
- [17] J.-S. Park, J. Kang, J.-H. Yang, W. Metzger, S.-H. Wei, Stability and electronic structure of the low- $\Sigma$  grain boundaries in CdTe: a density functional study, *New J. Phys.* 17 (2015) 013027, <http://dx.doi.org/10.1088/1367-2630/17/1/013027>.
- [18] S. Zaefferer, S.I. Wright, D. Raabe, Three-dimensional orientation microscopy in a focused ion beam-scanning electron microscope: a new dimension of microstructure characterization, *Metall. Mater. Trans. A* 39 (2008) 374–389, <http://dx.doi.org/10.1007/s11661-007-9418-9>.
- [19] J. Michael, L. Giannuzzi, Improved EBSD sample preparation via low energy Ga<sup>+</sup> FIB ion milling, *Microsc. Microanal.* 13 (2007) 926–927, <http://dx.doi.org/10.1017/S1431927607017196>.
- [20] J. Konrad, S. Zaefferer, D. Raabe, Investigation of orientation gradients around a hard laves particle in a warm-rolled Fe<sub>3</sub>Al-based alloy using a 3D EBSD–FIB technique, *Acta Mater.* 54 (2006) 1369–1380, <http://dx.doi.org/10.1016/j.actamat.2005.11.015>.
- [21] L.A. Giannuzzi, F.A. Stevie, A review of focused ion beam milling techniques for TEM specimen preparation, *Micron* 30 (1999) 197–204, [http://dx.doi.org/10.1016/S0968-4328\(99\)00005-0](http://dx.doi.org/10.1016/S0968-4328(99)00005-0).
- [22] J. Mayer, L.A. Giannuzzi, T. Kamino, J. Michael, TEM sample preparation and damage, *MRS Bull.* 32 (2007) 400–407, <http://dx.doi.org/10.1557/mrs2007.63>.
- [23] C.W. Rischau, C.S. Schnohr, E. Wendler, W. Wesch, Ion-beam-induced damage formation in CdTe, *J. Appl. Phys.* 109 (2011) 113531, <http://dx.doi.org/10.1063/1.3592265>.
- [24] C. Gretener, J. Perrenoud, L. Kranz, L. Kneer, R. Schmitt, S. Buecheler, et al., CdTe/CdS thin film solar cells grown in substrate configuration, *Prog. Photovoltaics Res. Appl.* 21 (2013) 1580–1586, <http://dx.doi.org/10.1002/pip>.
- [25] J.D. Major, R.E. Treharne, L.J. Phillips, K. Durose, A low-cost non-toxic post-growth activation step for CdTe solar cells, *Nature* 511 (2014) 334–337, <http://dx.doi.org/10.1038/nature13435>.
- [26] L. Kranz, C. Gretener, J. Perrenoud, R. Schmitt, F. Pianezzi, F. La Mattina, et al., Doping of polycrystalline CdTe for high-efficiency solar cells on flexible metal foil, *Nat. Commun.* 4 (2013) 2306, <http://dx.doi.org/10.1038/ncomms3306>.
- [27] A.J. Schwartz, M. Kumar, B.L. Adams, D.P. Field, Electron Backscatter Diffraction in Materials Science, <http://dx.doi.org/10.1007/978-0-387-88136-2>.
- [28] P.J. Konijnenberg, S. Zaefferer, S.B. Lee, A.D. Rollett, G.S. Rohrer, D. Raabe, Advanced methods and tools for reconstruction and analysis of grain boundaries from 3D-EBSD data sets, *Mater. Sci. Forum* 702–703 (2011) 475–478, <http://dx.doi.org/10.4028/www.scientific.net/MSF.702-703.475>.
- [29] C.V. Thompson, R. Carel, Texture development in polycrystalline thin films, *Mater. Sci. Eng. B* 32 (1995) 211–219, [http://dx.doi.org/10.1016/0921-5107\(95\)03011-5](http://dx.doi.org/10.1016/0921-5107(95)03011-5).
- [30] C. Cayron, Quantification of multiple twinning in face centred cubic materials, *Acta Mater.* 59 (2011) 252–262, <http://dx.doi.org/10.1016/j.actamat.2010.09.029>.
- [31] M.M. Nowell, S.I. Wright, M.A. Scarpulla, A.D. Compaan, X. Liuc, N.R. Paudel, et al., The correlation of performance in CdTe photovoltaics with grain boundaries, In: *Proceedings of the Conference Record of the 19th IEEE International Symposium Physics and Failure Analysis of Integrated Circuits*, Singapore, 2012, pp. 1–7. (<http://ieeexplore.ieee.org/lpdocs/epic03/wrapper.htm?arnumber=6306331>) (accessed 07.01.14).
- [32] H.R. Moutinho, R.G. Dhere, M.J. Romero, C.-S. Jiang, B. To, M.M. Al-Jassim, Electron backscatter diffraction of CdTe thin films: effects of CdCl<sub>2</sub> treatment, *J. Vac. Sci. Technol. A* 26 (2008) 1068, <http://dx.doi.org/10.1116/1.2841523>.
- [33] P.J. Konijnenberg, S. Zaefferer, D. Raabe, Assessment of geometrically necessary dislocation levels derived by 3D EBSD, *Acta Mater.* 99 (2015) 402–414, <http://dx.doi.org/10.1016/j.actamat.2015.06.051>.
- [34] C.V. Thompson, The yield stress of polycrystalline thin films, *J. Mater. Res.* 8 (1993) 237–238, <http://dx.doi.org/10.1557/JMR.1993.0237>.
- [35] G. Zoppi, K. Durose, S.J.C. Irvine, V. Barrioz, Grain and crystal texture properties of absorber layers in MOCVD-grown CdTe/CdS solar cells, *Semicond. Sci. Technol.* 21 (2006) 763–770, <http://dx.doi.org/10.1088/0268-1242/21/6/009>.
- [36] A. Romeo, D. Bätzner, H. Zogg, A. Tiwari, Recrystallization in CdTe/CdS, *Thin Solid Films* 361–362 (2000) 420–425, [http://dx.doi.org/10.1016/S0040-6090\(99\)00753-1](http://dx.doi.org/10.1016/S0040-6090(99)00753-1).
- [37] H. Masui, S.C. Cruz, S. Nakamura, S.P. Denbaars, Geometrical characteristics and surface polarity of inclined crystallographic planes of the wurtzite and zincblende structures, *J. Electron. Mater.* 38 (2009) 756–760, <http://dx.doi.org/10.1007/s11664-009-0777-4>.
- [38] S. Cho, A. DiVenere, G. Wong, J. Ketterson, J. Meyer, J.-I. Hong, Growth-mode modification of Bi on CdTe(111)A using Te monolayer deposition, *Phys. Rev. B* 58 (1998) 2324–2328, <http://dx.doi.org/10.1103/PhysRevB.58.2324>.
- [39] H. Wu, L. Wu, J. Hui, X. Jin, S. Du, Effective biaxial modulus and strain energy density of ideally (hkl)-fiber-textured cubic polycrystalline films, *Appl. Surf. Sci.* 254 (2008) 4067–4074, <http://dx.doi.org/10.1016/j.apsusc.2007.12.054>.
- [40] E. Deligoz, K. Colakoglu, Y. Ciftci, Elastic, electronic, and lattice dynamical properties of CdS, CdSe, and CdTe, *Phys. B Condens. Matter* 373 (2006) 124–130, <http://dx.doi.org/10.1016/j.physb.2005.11.099>.
- [41] G. Gottstein, *Physical Foundations of Materials Science*, Springer Berlin Heidelberg, Heidelberg, Berlin (2004) <http://dx.doi.org/10.1007/978-3-662-09291-0>.
- [42] S. Adachi, *Properties of Group-IV, III-V and II-VI Semiconductors*, John Wiley & Sons, Ltd., Chichester, UK (2005) <http://dx.doi.org/10.1002/0470090340>.
- [43] S. Mnasri, S. Abdi-Ben Nasrallah, N. Sfina, N. Bouarissa, M. Said, Electronic, lattice vibration and mechanical properties of CdTe, ZnTe, MnTe, MgTe, HgTe and their ternary alloys, *Semicond. Sci. Technol.* 24 (2009) 095008, <http://dx.doi.org/10.1088/0268-1242/24/9/095008>.
- [44] J. Wang, N. Li, O. Anderoglu, X. Zhang, a Misra, J.Y. Huang, et al., Detwinning mechanisms for growth twins in face-centered cubic metals, *Acta Mater.* 58 (2010) 2262–2270, <http://dx.doi.org/10.1016/j.actamat.2009.12.013>.
- [45] V. Consonni, G. Feuillet, Effects of chlorine drag on the annealing-induced abnormal grain growth in polycrystalline CdTe, *J. Cryst. Growth* 316 (2011) 1–5, <http://dx.doi.org/10.1016/j.jcrysgro.2010.11.156>.